Journal of Power Sources 555 (2023) 232390

Contents lists available at ScienceDirect

Journal of Power Sources

journal homepage: www.elsevier.com/locate/jpowsour

Tuning synthesis parameters and support composition for high-performing and durable *core-shell* Pt–Ni carbon nitride electrocatalysts for the oxygen reduction reaction

Francesca Lorandi [a], Keti Vezzù [a,b], Angeloclaudio Nale [a], Gioele Pagot [a], Yannick H. Bang [a], Enrico Negro [a], Vito Di Noto [a,b,*]

[a] *Section of "Chemistry for the Technology" (ChemTech), Department of Industrial Engineering, University of Padova, Via Marzolo 9, I-35131, Padova, (PD), Italy*
[b] *Consorzio Interuniversitario per la Scienza e la Tecnologia dei Materiali (INSTM), Italy*

HIGHLIGHTS

- Hierarchical *core-shell* Pt–Ni ORR electrocatalysts (ECs) are obtained.
- Interplay between synthesis, properties, and performance of ECs is discussed.
- Hierarchical Pt–Ni ECs exhibit mass activities surpassing DOE targets.
- Hierarchical Pt–Ni ECs are more durable than Pt/C reference ECs.

GRAPHICAL ABSTRACT

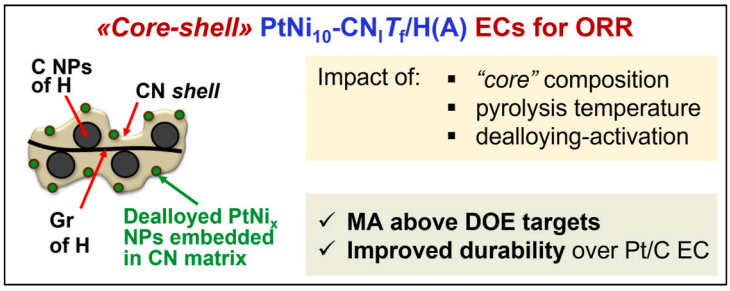

ARTICLE INFO

Keywords:
Proton exchange membrane fuel cells
Low-Pt electrocatalyst
Oxygen reduction reaction
Carbon nitride electrocatalyst
Core-shell electrocatalyst
Pt-Ni alloy electrocatalyst

ABSTRACT

This report presents the interplay between the synthesis parameters, physicochemical properties, and electrochemical performance of *core-shell* low-Pt electrocatalysts (ECs) for the oxygen reduction reaction (ORR) based on Pt_xNi active sites stabilized on a carbon nitride *shell*. The impact of the pyrolysis temperature (T_f), of the support *core* (**H**) composition and of an electrochemical dealloying-activation step on the EC morphology and on the accessibility and stability of the active sites are studied in detail. Three supports are employed based on carbon nanoparticles and/or graphene platelets. The ORR performance of activated ECs measured by cyclic voltammetry with the thin-film rotating ring-disk electrode approach is strongly affected by T_f and **H**. The best performing ECs are tested in single proton exchange membrane fuel cells under operating conditions. The simultaneous presence of graphene and carbon in **H** improves the dispersion of active sites, resulting in a vastly improved mass activity and durability in comparison with a benchmark state-of-the-art Pt/C EC.

* Corresponding author. Section of "Chemistry for the Technology" (ChemTech), Department of Industrial Engineering, University of Padova, Via Marzolo 9, I-35131, Padova, (PD), Italy.
E-mail address: vito.dinoto@unipd.it (V. Di Noto).

https://doi.org/10.1016/j.jpowsour.2022.232390
Received 5 August 2022; Received in revised form 5 November 2022; Accepted 9 November 2022
Available online 19 November 2022

1. Introduction

Fuel cells (FCs) are a crucial technology for both stationary and mobile applications in a decarbonized economy [1]. In particular, proton exchange membrane FCs (PEMFCs) operate at low temperatures (60–100 °C) with an energy conversion efficiency up to 60% or more. They are commonly used in FC electric vehicles, which are set to top 10 million by 2030 [1,2]. However, the reliance on critical raw materials (CRMs) such as platinum-group metals (PGMs), that are prone to trigger supply bottlenecks, and the limited durability of state-of-the-art PEMFCs inhibit the latter's commercialization and large-scale rollout.

The sluggish kinetics of the oxygen reduction reaction (ORR), that occurs at the cathode of a PEMFC, typically requires the introduction of a PGM-based electrocatalyst (EC) in the cathodic electrocatalytic layer [1,3]. The platinum loading is typically high, *ca.* 0.35 $mg_{Pt}{\cdot}cm^{-2}$. In a high-volume production scenario, the cost of the EC is projected to account for up to 60% of the stack cost of a PEMFC for heavy-duty vehicles [4]. Therefore, it becomes necessary to develop effective ECs with a low PGM loading and/or non-PGM ECs to curtail the costs (for instance, the ultimate cost target set by the U.S. Department of Energy, DOE, is 30 $\$/kW_{net}$) [5]. Furthermore, PGMs are part of the Critical Raw Materials list compiled by the European Union, with a moderate supply risk [6]. In fact, PGMs are very scarce in Earth's crust and their geographical distribution is very uneven, with the vast majority of Pt (71%) coming from South Africa [6]. Thus, it is of the utmost importance to decrease the Pt loading in the cathodic electrocatalytic layer to $<0.1\ mg_{Pt}{\cdot}cm^{-2}$, at the same time ensuring a device durability of 8000 h for mobile applications [1,5].

State-of-the-art ECs for the ORR consist of Pt nanoparticles supported on carbon black; they are typically indicated as Pt/C ECs [3,7]. The carbon support has the advantages of low cost, high electrical conductivity and high surface area. However, the performance of commercial Pt/C ECs tends to rapidly deteriorate due to a variety of phenomena, including the corrosion of the carbon support, detachment of Pt NPs and their coalescence with consequent loss of specific surface area [8–10]. One of the most effective approaches to simultaneously improve EC activity and durability while decreasing Pt loading is alloying Pt with other transition metals [11,12]. It is widely claimed that Pt alloying changes the binding strength of ORR intermediates with the surface of active sites, which can result in a decreased ORR overpotential and improved performance [7,13]. Nevertheless, the long-term stability of Pt-alloy-based ECs is often not satisfying, as dealloying occurs under the harsh FC operating conditions, causing oxidation and dissolution of the non-noble metals.

To enhance the EC durability, it becomes critical to tune the nature and morphology of the support [14]. The development of a carbon nitride (CN) matrix is a highly promising strategy to extend EC lifetime, as nitrogen atoms are embedded in the carbon support and help forming *"coordination nests"* for metal-based nanostructures [3,15]. The strong interactions between active sites and the CN-based support inhibit particle detachment and agglomeration. Moreover, N atoms promote the ORR kinetics through bifunctional and electronic effects [3,16]. A relatively high loading of N atoms (>5 wt%) can further improve the EC tolerance to contaminants [3,17]. On the other hand, a high N content increases the ohmic drops and worsen the performance if compared to CN-based ECs with a low N content (<5 wt%), wherein N atoms are mostly located in proximity of the active sites [17].

The morphology of a Pt-based EC for the ORR determines the accessibility of active sites and the utilization of Pt [3,7]. A *core-shell* morphology comprising a Pt-based *shell* surrounding a less-expensive, conductive *core*, offers a multiplicity of tailorable features to enhance the activity and durability of the EC [18]. CN-based ECs can be designed with a *core-shell* morphology, whereby the CN matrix stabilizing the metal active sites forms a *shell* around a conductive carbon *core*. Simple and scalable protocols have been developed in our laboratory for the synthesis of both low-PGM and PGM-free *core-shell* CN-based ECs [3,17,19,20], enabling to screen relatively large families of these materials and optimize the synthetic conditions to achieve targeted performance and durability.

Herein, we report a family of *core-shell* CN-based low-Pt ECs, where the CN-based *shell* supports ORR-active Pt-based NPs also comprising Ni as the *"co-catalyst"*, which improves the kinetics through both electronic and bifunctional effects. Such effects include the promotion of the first electron transfer from the EC to the incoming O_2 molecule and the facilitated desorption of the ORR products [21]. Ni was specifically selected as the *"co-catalyst"* among the different first-row transition metals since it exhibits quite a low reduction potential in acidic conditions [22]. Thus, excess Ni is easily etched during the final electrochemical dealloying and activation process yielding the final ECs. In addition, traces of Ni leached during long-term EC operation in single PEMFC: (i) will promote much less than Fe the formation of oxygen radical species able to accelerate the degradation of the device [23]; (ii) differently from Cu, will not re-deposit at the anode upon migration through the proton-exchange membrane [24]. The N content in the CN *shell* is kept below 5 wt% to avoid excessive ohmic drops. The EC preparation protocol (Scheme 1) includes: (i) the synthesis of a nanocomposite hybrid inorganic-organic precursor; (ii) a multistep pyrolysis process yielding pristine ECs, denoted as $PtNi_{10}$-CN_l***T*****$_f$/H**, where Pt and Ni are present in a molar ratio equal to *ca.* 1/10, the subscript *l* indicates a low N content, T_f corresponds to the final pyrolysis temperature, and **H** indicates the support *core*; and (iii) an electrochemical dealloying and activation process (A) to form activated ECs, *i.e.* $PtNi_{10}$-CN_l***T*****$_f$/H**(A). The dealloying-activation step enables to selectively remove the metal with a lower reduction potential at equilibrium, *i.e.* Ni, establishing the final morphology and ORR activity of the active sites [25,26]. The final pyrolysis temperature is set to either $T_f = 600$ or 900 °C; 3 different supports are explored: (i) carbon NPs (**H = C**); (ii) graphene layers (**H = Gr**); and (iii) a blend of carbon and graphene layers in a 1/1 wt ratio (**H = (C + Gr)**). The aim of this work is to study the interplay between the EC composition, T_f and the dealloying-activation step on the electrochemical performance measured both *ex situ* and *in situ* in single PEMFC. This goal is achieved by analyzing and comparing the structure, composition, morphology and thermal stability of pristine and activated ECs. The electrochemical performance of $PtNi_{10}$-CN_l***T*****$_f$/H**(A) is evaluated by cyclic voltammetry with the thin-film rotating ring-disk electrode (CV-TF-RRDE) [27,28] method in both acidic and alkaline media. *Ex situ* durability in an acidic medium is also explored. Membrane-electrode assemblies (MEAs) fabricated using the most promising ECs are tested in single PEMFCs in operating conditions. Superior performance is determined for $PtNi_{10}$-CN_l**900/H**(A) in comparison to a Pt/C reference (Pt/C ref.) EC. The inclusion of Gr in **H** promotes the accessibility of active sites and the establishment of interactions with the support, while the dealloying-activation step effectively modulates the physicochemical properties of the ECs and yields active sites exhibiting an outstanding ORR kinetics.

2. Experimental

2.1. Procedure for the synthesis of pristine ECs with H = C

The ECs reported in this work were synthesized according to a protocol described in the scientific and technical literature [3,29], based on the impregnation of the conductive support **H** with a zeolitic inorganic-organic polymer electrolyte (Z-IOPE). Briefly, 133.4 mg of sucrose were dissolved into the minimum amount of water (*ca.* 1 mL), yielding a clear viscous solution. Separately, 400 mg of K_2PtCl_4 were dissolved into the minimum amount of water (*ca.* 1 mL), forming a deep red solution. The viscous sucrose solution was added dropwise, under vigorous stirring, into the deep red solution of K_2PtCl_4. Then, 533.5 mg of Vulcan™ XC-72R were added, and the system was extensively homogenized by stirring and ultrasonication, yielding a homogeneous black dispersion. Using the same protocol, a second dispersion was

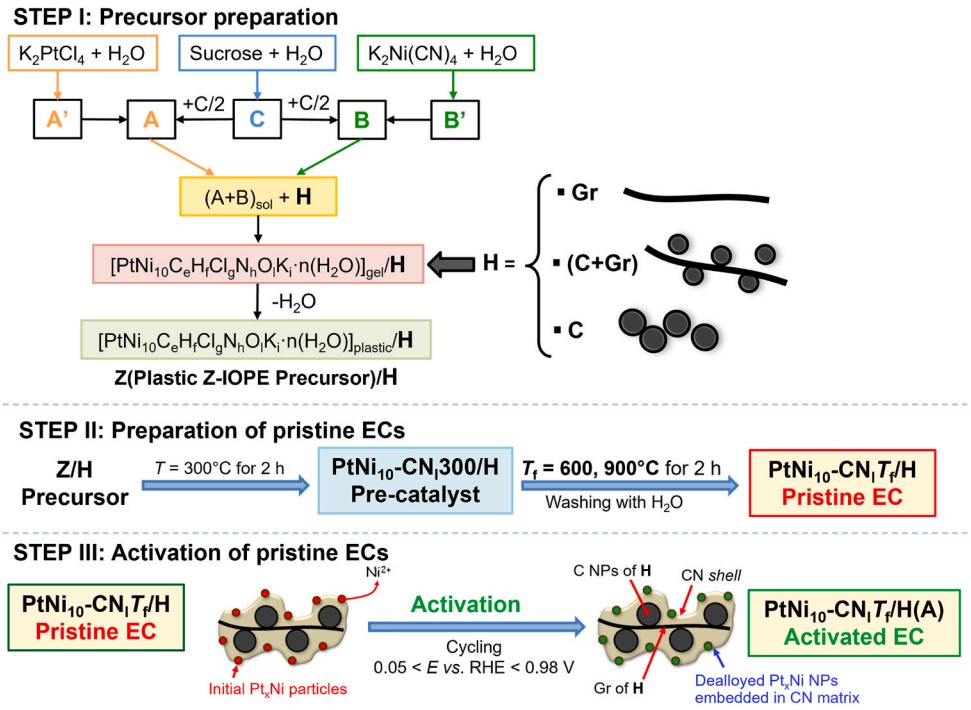

Scheme 1. Protocol for the preparation of *core-shell* CN-based Pt–Ni electrocatalysts, modulating the composition of the support *core* (**H**) and the temperature of the main pyrolysis step (T_f). Z-IOPE indicates the zeolitic inorganic organic polymer electrolyte formed during the first step (see Section 2.1).

prepared, where K_2PtCl_4 was replaced with 332.4 mg of $K_2Ni(CN)_4{\cdot}xH_2O$. The dispersion comprising K_2PtCl_4 was added dropwise, under vigorous stirring, to the dispersion containing $K_2Ni(CN)_4{\cdot}xH_2O$. The product was extensively homogenized by sonication, stirred for 24 h, and let to rest for additional 48 h; afterwards, it was treated overnight at 120 °C in an oven to remove most of the water. During these processes, networking reactions occurred where the precursor components crosslinked and underwent sol → gel and gel → plastic transitions. The result was a plastic Z-IOPE material (Z) that formed a 3D network *shell* homogeneously covering **H** (*i.e.* yielding a Z/**H** nanocomposite precursor). The black solid Z/**H** was transferred into a quartz tube, where it underwent a multi-step thermal treatment: (i) 300 °C for 2 h; and (ii) T_f = 600 or 900 °C for 2 h. The entire treatment was carried out under a dynamic vacuum of 10^{-1} mbar. The product was then: (i) washed three times with water; (ii) treated with a 10 vol% aqueous solution of H_2O_2; and (iii) dried overnight in an oven at T = 120 °C. After this sequence of operations, the pristine EC was obtained.

Two different pristine ECs were obtained with the described procedure: $PtNi_{10}$-CN_l**600/C** and $PtNi_{10}$-CN_l**900/C**. Labelling of the ECs is carried out in compliance with the indications provided in Section 1.

2.2. Procedure for the synthesis of pristine ECs with H = Gr and (C + Gr)

The Gr support was prepared as previously reported [19,30]. Briefly, 2 g of graphene nanoplatelets (GNPs) were suspended into 30 mL of HNO_3 under vigorous stirring. 30 mL of H_2O_2 were added dropwise. The suspension was stirred for 12 h at room temperature, then filtered on a Büchner funnel and extensively washed until a neutral pH was measured for the mother waters. The resulting solid was dried in a ventilated oven at T = 150 °C. The obtained product was then used to prepare the $PtNi_{10}$-$CN_l$$T_f$/**Gr** and $PtNi_{10}$-$CN_l$$T_f$/**(C + Gr)** pristine ECs by adopting a procedure similar to that described above for $PtNi_{10}$-$CN_l$$T_f$/**C**. The main difference is that Vulcan™ XC-72R was replaced with either the graphene support, **Gr**, or with a mixture of graphene and Vulcan™ XC-72R in a 1:1 Gr:C weight ratio **(C + Gr)**, which were mixed with the sucrose solutions containing either K_2PtCl_4 or $K_2Ni(CN)_4{\cdot}xH_2O$. Four different pristine ECs were obtained with the described procedure: $PtNi_{10}$-CN_l**600/Gr**, $PtNi_{10}$-CN_l**900/Gr**, $PtNi_{10}$-CN_l**600/(C + Gr)**, $PtNi_{10}$-CN_l**900/(C + Gr)**. Labelling of the ECs is carried out in compliance with the indications provided in Section 1.

2.3. Procedure for the electrochemical activation of pristine ECs

Pristine ECs were electrochemically activated, following a 3-step procedure: (i) inks of $PtNi_{10}$-$CN_l$$T_f$/**H** were painted on carbon papers that were used to obtain gas-diffusion cathodes (GDCs); (ii) GDCs were extensively cycled in a half-cell configuration, in a potential range of 0.05–0.98 V *vs.* RHE in 0.1 M $HClO_4$, under alternating inert and oxidizing (O_2) atmospheres. According to the Pourbaix diagram [22], at the solution pH (nominally 1) and within the selected potential range Ni was etched, while Pt was unaffected. Therefore, one of the main outcomes of the activation procedure was the removal of the labile metal species that were not strongly interacting with the support. Upon cycling the activated ECs, denoted as $PtNi_{10}$-$CN_l$$T_f$/**H**(A), were extracted from the GDCs. Such activated ECs were characterized to analyze their chemical composition, thermal stability and physicochemical properties. Finally, the activated GDCs were used to fabricate membrane-electrode assemblies (MEAs) tested in operating conditions.

2.4. Electrochemical measurements

Electrochemical measurements were carried out with the CV-TF-RRDE method according to a previously reported procedure [31,32]. Briefly, each pristine EC was mixed with Vulcan™ XC-72R in a 2:1 EC: XC weight ratio and ground in a mortar, until a homogeneous powder was obtained. Suitable amounts of doubly distilled water, isopropanol and a commercial Nafion 1100 dispersion were used to suspend these mixtures, yielding the EC inks. The Pt/C ref. EC did not undergo any mixing with Vulcan™ XC-72R and grinding but was suspended in a similar mixture of solvents and Nafion dispersion. A 12 μL drop of each ink was pipetted onto the glassy carbon (GC) disk of a RRDE tip to obtain a uniform electrode film [33]. The platinum loading on the GC disk of the RRDE tip was fixed to 15 $\mu g_{Pt}{\cdot}cm^{-2}$ for each sample. The electrochemical instrumentation and setup, and the procedure employed in the

measurements are reported in detail elsewhere [32]. Briefly, the RRDE used as the working electrode was mounted on a model 636 rotator (Pine Research Instrumentations). The collection efficiency of the Pt ring was equal to 0.39. The experiments were performed with a Bio-Logic VSP multichannel potentiostat/galvanostat. Initially, the electrode was cycled between $E = 0.05$ and 1.05 V *vs.* reversible hydrogen electrode (RHE) in an acid solution of 0.1 M $HClO_4$, under pure O_2, at a temperature of 25 °C and a sweep rate of 20 $mV{\cdot}s^{-1}$, as the RRDE tip was rotated at 1600 rpm. Cycling was performed until the voltammograms became stable. The acid solution was then discarded and replaced with a new 0.1 M $HClO_4$ solution, wherein the final electrochemical measurements were collected in the conditions described above. Subsequently, the acid solution was replaced with a 0.1 M KOH solution and the electrode was cycled between $E = 0.05$ and 1.05 V *vs.* RHE, in pure O_2, at 20 $mV{\cdot}s^{-1}$, while the rotation was set at 1600 rpm. The generation of H_2O_2 is monitored at the ring electrode, kept at $E = 1.2$ V *vs.* RHE [34]. The faradaic ORR currents were obtained upon subtraction of voltammograms collected in Ar-saturated solutions, under otherwise identical conditions to the ORR measurements. iR-correction was carried out as described elsewhere [35]. The disk currents were normalized on the geometric area of the GC. The reference electrodes for the acid and alkaline environments were $Hg/HgSO_4/K_2SO_4$(sat.) and Hg/HgO/KOH (aq.) (0.1 M), respectively. Before each measurement, the exact determination of the RHE potential was carried out as described elsewhere [36]. The counter electrode was a Pt wire. CO stripping measurements were performed by polarizing the electrode at 0.1 V *vs.* RHE for 10 min in a CO-saturated solution at $T = 25$ °C. Afterwards, the cell was purged with Ar for 20 min, while the working electrode polarization was maintained at 0.1 V *vs.* RHE. The CO molecules irreversibly adsorbed on the EC active sites were then stripped by linearly increasing the potential of the working electrode from 0.1 to 1.15 V *vs.* RHE at 20 $mV{\cdot}s^{-1}$. Then, the electrode was further cycled between 0.05 and 1.15 V *vs.* RHE at 20 $mV{\cdot}s^{-1}$ in a pure Ar atmosphere; the obtained profiles were subtracted from the CO_{ad} stripping trace to obtain the net stripping currents through which the electrochemically active surface area (ECSA) was evaluated [32]. The durability test is carried out according to a testing protocol based on continuous cycling in inert atmosphere at a potential range between 0.6 and 1.0 V *vs.* RHE and a scan rate of 50 $mV{\cdot}s^{-1}$. ORR and CO stripping profiles are evaluated after 10, 100, 1000, 3000, 10000 and 20000 cycles [37].

2.5. Membrane-electrode assemblies preparations and tests in single PEMFC

The MEAs were fabricated according to a previously described, catalyst-coated substrate procedure [38]. In brief, commercial Nafion112™ membranes (Ion Power) were employed as the membrane, and GDS1120 carbon paper (Ballard Material Products) was used as the gas-diffusion support for the electrocatalytic layers. The membranes were cleaned through a 3-step procedure: (i) immersion in 3 wt% H_2O_2 for 1 h; (ii) immersion in 1 M H_2SO_4 for 1 h; and (iii) treatment in doubly distilled water for 1 h. All treatments were carried out at 80 °C. The anode electrocatalyst was EC-20 (Pt/C ref. with nominal Pt loading of 20 wt% on Vulcan XC-72R support), with a platinum loading of 0.4 $mg{\cdot}cm^{-2}$. The cathode electrocatalytic layers were obtained by diluting the ECs with XC-72R in a 1:1 wt ratio. The platinum loading in each cathodic electrocatalytic layer was 0.1 $mg{\cdot}cm^{-2}$, and the overall Nafion/C mass ratio was equal to 0.6. The Pt loading on the cathode was selected on the basis of the requirements set by the U.S. DOE for advanced MEAs fed on direct hydrogen [5]. The electrocatalytic inks were drop-coated on the gas-diffusion supports, yielding the catalyst-coated gas diffusion electrodes (GDEs). The platinum loading at the cathode electrode was measured starting from the weight difference between the dry cathode electrode and the blank gas diffusion support, taking into account the wt% of Pt in the EC and the overall formulation of the electrocatalytic layer. Hot-pressing was used to fuse the GDEs onto the membranes. A back pressure (BP) of the reagents equal to either 4 or 1 bar was used during single fuel cell tests, performed as described elsewhere [32]. Further details on the employed instruments and characterization methods are available in the Supporting Information.

3. Results and discussion

The objective of the present study is to analyze the interplay between the composition, structure, morphology and electrochemical performance of *core-shell* CN-based Pt–Ni ECs upon systematic variation of the type of support *core* and of key synthetic parameters. In particular, it is discussed how the composition of **H**, the temperature of the main pyrolysis step (T_f) and the EC activation affect the features of the active sites. Therefore, three supports are considered: (i) carbon NPs with a diameter of ~30–50 nm (**H = C**); (ii) graphene layers (**H = Gr**); and (iii) a blend of carbon and graphene in a 1:1 wt ratio (**H = (C + Gr)**). Graphene is characterized by a high electron conductivity, a large surface area (up to 2500 $cm^2{\cdot}g^{-1}$), a high thermal stability and facile doping with heteroatoms [39]. Thus, graphene and related materials have been broadly employed as support material for fuel cell ECs [40–42]. Our group developed hierarchical PGM-free ECs composed of Gr nanoplatelets in the *core* and CN-based *shells*, exhibiting a high ORR activity in alkaline medium [19,43]. In the low-Pt ECs reported here, Gr is introduced in **H** to evaluate its effect on: (i) the morphology of the ECs; and (ii) the accessibility of Pt_xNi active sites and on their interactions with C- and N-ligands.

The procedure adopted for the synthesis of *core-shell* ECs is well-established and consists of 3 main steps (Scheme 1). First, a nanocomposite zeolitic hybrid organic-inorganic polymer electrolyte (Z-IOPE) precursor (Z/**H**) is prepared by combining: (i) a Pt coordination compound bearing good leaving groups coordinated to the Pt center; (ii) a Ni complex with CN groups; (iii) a sucrose binder; and (iv) the support **H**. The labile groups in the Pt complex are displaced by either the cyanonickelate ligands or the –OH groups present in the binder and on the surface of **H** (C NPs and/or Gr). This results in a 3D crosslinked *shell* that uniformly covers **H**. The optimal mass ratio between the sucrose binder and C NPs to obtain a compact CN *shell* was previously determined for a different family of *core-shell* ECs as binder/C NPs 1:1 [20]. Therefore, herein a binder/**H** mass ratio of 1:1 is adopted. This procedure ensures that Z/**H** precursors present: (i) metal sites covalently bound to C and N atoms of the CN *shell*; and (ii) N atoms mostly located close to metal species. Then, Z/**H** precursors undergo a multi-step pyrolysis process (see Experimental Section). The initial, low-temperature pyrolysis gradually removes low-molecular-weight species and creates an infusible structure of the Z *shell*, stabilizing the morphology. The purpose of the successive, higher-temperature pyrolysis is to: (i) trigger the nucleation and growth of metal NPs; (ii) promote the establishment of strong interactions between the metal NPs and the support, creating an effective CN-*shell* where the metal NPs bearing active sites are embedded in *coordination nests*; (iii) graphitize the matrix to improve the conductivity; and (iv) raise microporosity to facilitate the access of reactants to the active sites [32]. The impact of this final pyrolysis temperature (T_f) is evaluated by employing either $T_f = 600$ °C or 900 °C.

The last step is the electrochemical dealloying-activation of the ECs. This step further removes labile species, improving the accessibility of the active sites and modulating the chemistry and morphology of the ECs.

3.1. Chemical composition of pristine and activated $PtNi_{10}$-CN_lT_f/H

The bulk chemical composition of pristine $PtNi_{10}$-$CN_l\boldsymbol{T_f}$/**H** is determined by inductively-coupled plasma atomic optical emission spectroscopy (ICP-OES) and elemental analysis (Tables S1 and S2). The molar ratio between H and C atoms (n_H/n_C, Fig. 1A) is a measure of the graphitization degree of the CN *shell*, which increases as T_f is raised. In fact, n_H/n_C is *ca.* 10 times lower than the nominal value when T_f =

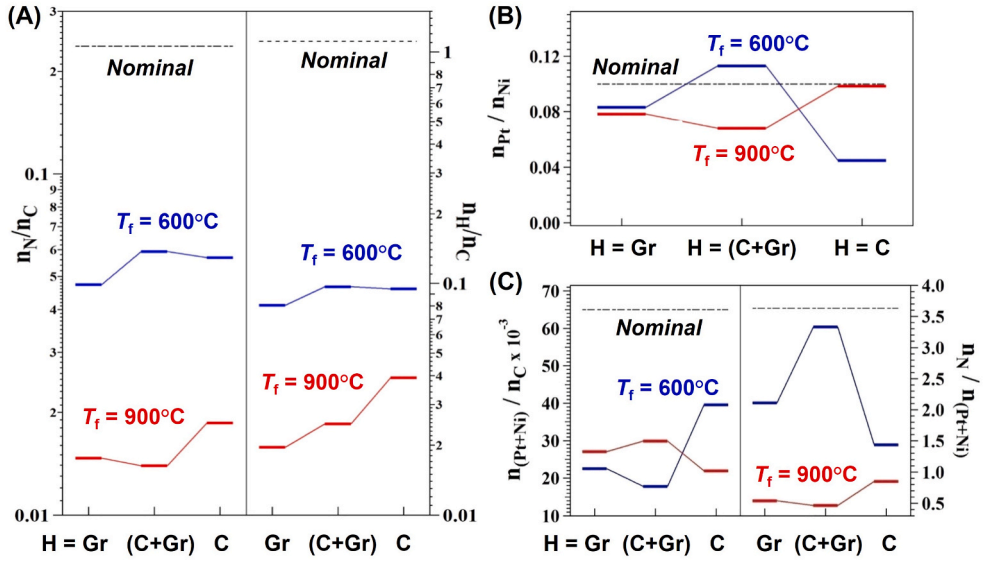

Fig. 1. Composition of the developed pristine ECs in terms of: (A) C, H, N atoms; (B,C) metal species, as a function of the nature of the support **H** = **Gr**, **(C + Gr)**, **C**, and of the second pyrolysis temperature, T_f = 600 (blue lines) or 900 °C (red lines). (For interpretation of the references to colour in this figure legend, the reader is referred to the Web version of this article.)

600 °C, and further decreases by 2.5–4 times in $PtNi_{10}$-CN_l**900/H**. The lowest values of n_H/n_C, thus the highest graphitization degrees, are obtained for $PtNi_{10}$-CN_l**900/Gr** and $PtNi_{10}$-CN_l**900/(C + Gr)**. Conversely, no substantial support effect is detected on the graphitization degree of the ECs treated at lower T_f. A similar trend is observed for the molar ratio between N and C atoms, n_N/n_C (Fig. 1A), indicative of improved graphitization of the CN *shell* at higher T_f. These observations are in agreement with recent *in-situ* analysis of the pyrolysis temperature effect on Fe-based carbon nitride ECs, showing that $T > 870$ °C is needed to trigger the graphitization and reduction step [44].

Concerning metal species, the ratio between Pt and Ni atoms, n_{Pt}/n_{Ni} (Fig. 1B), is only slightly lower than the nominal value and it is mostly unaffected by **H**, indicating that the metal stoichiometry is always quite well-controlled during the EC synthesis. On the other hand, $n_{(Pt + Ni)}/n_C$ (Fig. 1C) is lower than the nominal value, since only active sites strongly interacting with the support are preserved during the synthesis, while labile metal species are removed. This is a fundamental aspect in order to obtain materials endowed with a high chemical and electrochemical stability, and a long cycle life. The ratio between N atoms and metal atoms, $n_N/n_{(Pt + Ni)}$ (Fig. 1C), is higher for $PtNi_{10}$-CN_l**600/H** compared to $PtNi_{10}$-CN_l**900/H** ($n_N/n_{(Pt + Ni)} > 1.4$ and <0.7, respectively), indicating that the active sites are less coordinated by N-ligands in the ECs treated at higher T_f.

The bulk composition of pristine ECs is also analyzed by energy dispersive X-ray spectroscopy (EDX), as well as the bulk composition of the ECs upon activation (Table S3). Moreover, the surface composition of both pristine and activated ECs is determined by X-ray photoelectron spectroscopy (XPS, Table S4). For pristine ECs, a higher n_N/n_C is always measured on the EC surface compared to the bulk (Fig. 2A), indicating that N atoms are concentrated in the surface of the *shell*. Upon

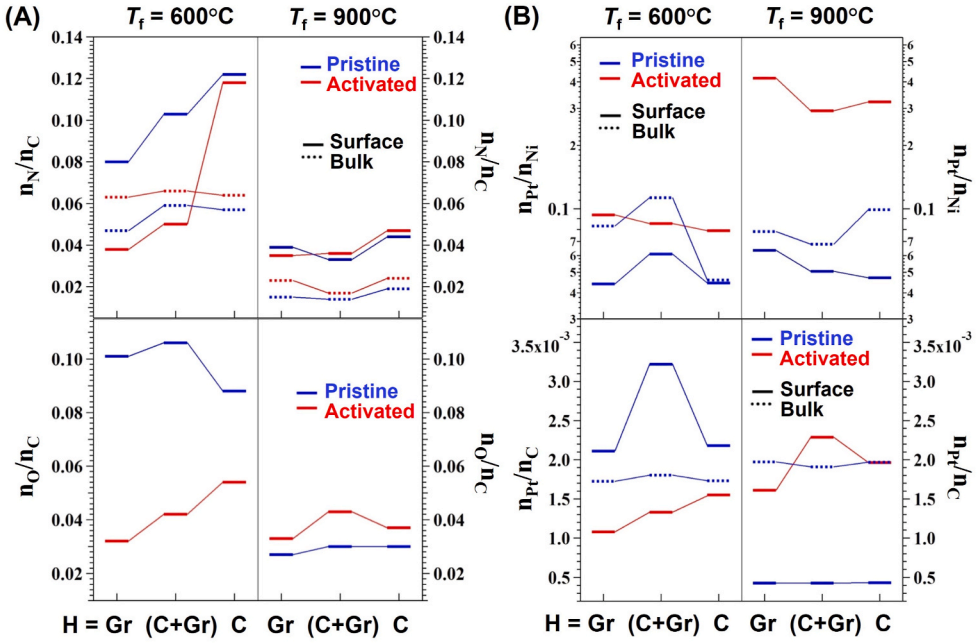

Fig. 2. Comparison between surface (solid lines) and bulk (dotted lines) composition of the developed *core-shell* pristine (blue lines) and activated (red lines) ECs, in terms of: (A) N,C,O atoms; (B) metal species, as a function of the nature of the support (**H** = **Gr**, **(C + Gr)**, **C**), of the second pyrolysis temperature (T_f = 600 or 900 °C), and of the electrochemical activation of the ECs. (For interpretation of the references to colour in this figure legend, the reader is referred to the Web version of this article.)

activation, $PtNi_{10}$-CN_l**600/H**(A) ECs exhibit a sharp decrease in n_N/n_C on the surface when Gr is present in **H**, becoming even lower than the same parameter in the bulk. Thus, the activation contributed to increase the graphitization of the CN matrix. On the other hand, for the ECs treated at T_f = 900 °C, n_N/n_C is nearly unchanged upon activation. Regardless of T_f, n_N/n_C is higher for **H** = C NPs, indicating that this support improves the retention of N atoms to the outer part of the *shell*. At the same time, n_O/n_C on the surface of pristine ECs is much larger when T_f = 600 °C (Fig. 2A), indicating that T_f = 900 °C promotes the reduction of the CN *shell* through the elimination of the O-based species. Upon activation, n_O/n_C greatly decreases in $PtNi_{10}$-CN_l**600/H**(A), but slightly increases in $PtNi_{10}$-CN_l**900/H**(A). This suggests that activation etches oxygen-rich species from the EC surface at T_f = 600 °C, while triggers a modest oxidation of the CN *shell* at T_f = 900°C.

Focusing on metal species (Fig. 2B), the surface n_{Pt}/n_{Ni} ratio increases upon activation, as the latter effectively removes labile Ni species. The increase in n_{Pt}/n_{Ni} is much larger for the ECs treated at T_f = 900 °C, where surface values of n_{Pt}/n_{Ni} = 0.29–0.4 are obtained, while the bulk values are lower (0.06–0.1). Among the activated ECs treated at high temperature, $PtNi_{10}$-CN_l**900/(C + Gr)**(A) exhibits the lowest value of n_{Pt}/n_{Ni}, indicating that the active sites are richer in Ni atoms. Among activated ECs treated at T_f = 600 °C, n_{Pt}/n_{Ni} is lower when C is present in **H**. In addition, n_{Pt}/n_C on the surface decreases upon activation to values lower than in the bulk, when T_f = 600 °C (Fig. 2B). In contrast, when T_f = 900 °C, n_{Pt}/n_C on the surface of pristine ECs is much lower than in $PtNi_{10}$-CN_l**600/H**, but it is dramatically raised upon activation. The described trends show that: (i) in pristine ECs the CN *shell* is enriched in Ni species; (ii) the activation procedure removed labile Ni species and other derivatives loosely interacting with the Pt_xNi active sites; and (iii) the higher pyrolysis temperature promotes the migration of Pt to the outer surface of the CN *shell* that is enriched of Pt_xNi NPs and nanoaggregates, thus improving the exposure of active sites.

High-resolution XPS (HR-XPS) analysis was adopted to study the oxidation states of the metal species (Fig. 3). The HR-XPS profiles displayed in Fig. 3 were decomposed in compliance with the literature [45, 46], allowing for the quantification of the incidence of the different oxidation states of Pt and Ni. Sample decompositions of HR-XPS profiles are shown in Fig. S1 and Fig. S2. The decomposition of Pt4f peaks reveals three components, ascribed to Pt(0) (B.E. of 71.3 eV) and two oxidized Pt species, lumped together under a *"Pt(Ox)"* label (B.E. of 72.5 eV and 73.5 eV, respectively). In pristine ECs, platinum is mostly present as Pt(Ox) in $PtNi_{10}$-CN_l**600/H**, and as Pt(0) in $PtNi_{10}$-CN_l**900/H** (see the left panels of Fig. 3). Specifically, $PtNi_{10}$-CN_l**600/H** and $PtNi_{10}$-CN_l**900/H** include 19 and 66 at% of Pt(0) (see Fig. S3). $PtNi_{10}$-CN_l**600/H** only exhibits Ni(II) (see the right panels of Fig. 3). The decomposition of $PtNi_{10}$-CN_l**600/H** Ni2p profiles reveals three components, ascribed to: (i) Ni oxides (B.E. of 855.5 eV); (ii) Ni hydroxides (B.E. of 856.7 eV); and (iii) satellite peaks (B.E. of 861.6). The incidence of Ni oxides and Ni hydroxides is 74 at% and 26 at%, respectively (see Fig. S4 and Fig. S5). The HR-XPS Ni2p spectra of $PtNi_{10}$-CN_l**900/H** display the same components as $PtNi_{10}$-CN_l**600/H**; in addition, $PtNi_{10}$-CN_l**900/H** includes 18 at% of metallic Ni (B.E. of 854 eV, see Fig. S6). An intense Ni3p peak is always detected very close to the Pt4f peaks (see the left panels of Fig. 3 and Fig. S1). The latter strongly decreases in intensity upon electrochemical activation, nearly disappearing in activated ECs treated at T_f = 900 °C. This evidence further confirms that labile Ni species are removed. Activation does not affect significantly the incidence of Pt(0) (see Fig. S3). On one hand, this indicates that a pyrolysis temperature of 600 °C is insufficient to reduce most of Pt(Ox) to Pt(0). On the other hand, HR-XPS proves that Pt sites are not removed during the activation step because of their strong coordination with the CN matrix. Activation hardly affects the incidence of the Ni components of $PtNi_{10}$-CN_l**600/H.** On the other hand, in the case of $PtNi_{10}$-CN_l**900/H,** activation: (i) reduces significantly the incidence of Ni hydroxides (from 34 at% to 20 at%, see Fig. S5); and (ii) does not influence the incidence of Ni(0) (which rises slightly from 18 at% to 21 at%, see Fig. S6). These results are interpreted admitting that in $PtNi_{10}$-CN_l**900/H**: (i) Ni(0) species are present due to a stabilizing spillover effect from neighboring Pt(0) species, that are found with a similar and very high incidence on the surface of both pristine and activated samples (see Fig. S3); and (ii) the stabilizing spillover effect preferably extends from Pt(0) to Ni(0) and Ni oxides, while Ni hydroxides (that form fewer chemical bonds with the bulk) are less protected and more exposed to electrochemical etching. In $PtNi_{10}$-CN_l**600/H,** activation etches both Ni oxides and Ni hydroxides practically at the same rate as the surface concentration of Pt(0) (19 at%, see Fig. S3) is likely not sufficient to establish a strong enough stabilizing spillover effect.

Finally, the surface concentration of carboxyl groups is lower for the ECs treated at higher T_f, and it decreases upon activation when T_f = 600 °C (Figs. S7 and S8). A similar trend is observed for pyridinic nitrogens and hydroxyl groups, further confirming that T_f = 900 °C promotes the graphitization of the CN *shell*. Overall, the temperature of the main pyrolysis step and electrochemical activation are crucial to modulate the structure and composition of the CN *shells* and of the Pt_xNi NPs and nanoaggregates embedded therein.

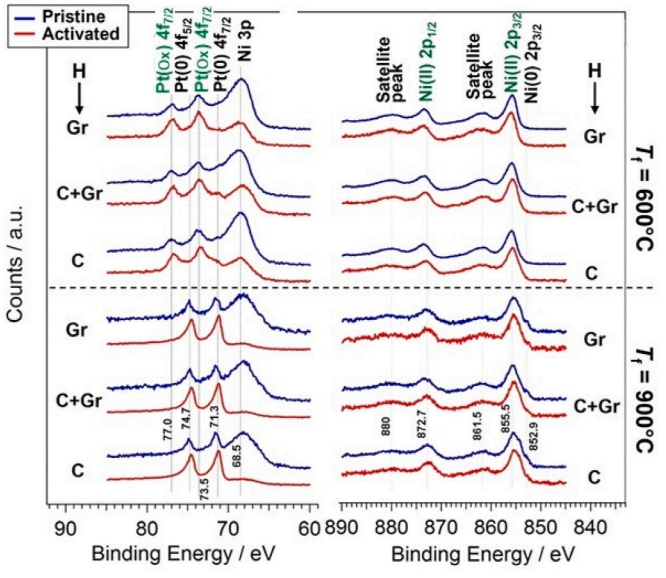

Fig. 3. Oxidation states of Pt and Ni species on the surface of the core-shell pristine (blue lines) and activated (red lines) ECs, determined by HR-XPS. (For interpretation of the references to colour in this figure legend, the reader is referred to the Web version of this article.)

3.2. Thermal stability in oxidizing and inert atmosphere

The thermal stability of the ECs is studied by means of high-resolution thermogravimetric analysis (HR-TGA) under either an oxidizing (Fig. 4) or inert (Fig. S9) atmosphere. Under oxidizing air atmosphere, 3 main mass losses are observed (Fig. 4): (i) the first at T_I ~400 °C is attributed to the degradation of the CN matrix; (ii) the second at T_{II} ~550 °C corresponds to the degradation of C; and (iii) the last at T_{III} ~650 °C to the degradation of Gr. This attribution is based on the comparison with the mass loss profiles of the Pt/C ref. EC and of the **H** supports prior to any further treatment. The presence of Gr in the *core* enhances not only the stability of the *core* itself, but also that of the CN matrix, as T_I increases in the order **H** = **C** < **(C + Gr)** < **Gr**. Moreover, T_I is *ca.* 50 °C higher for pristine ECs treated at T_f = 900 °C, compared to $PtNi_{10}$-CN_l**600/H**. In these latter ECs, T_I rises by 50–100 °C upon activation. Therefore, both high T_f and the activation process enhances the graphitization of the CN *shell*, in agreement with the composition analysis. For $PtNi_{10}$-CN_l**600/H**, T_{II} and T_{III} also increase upon activation.

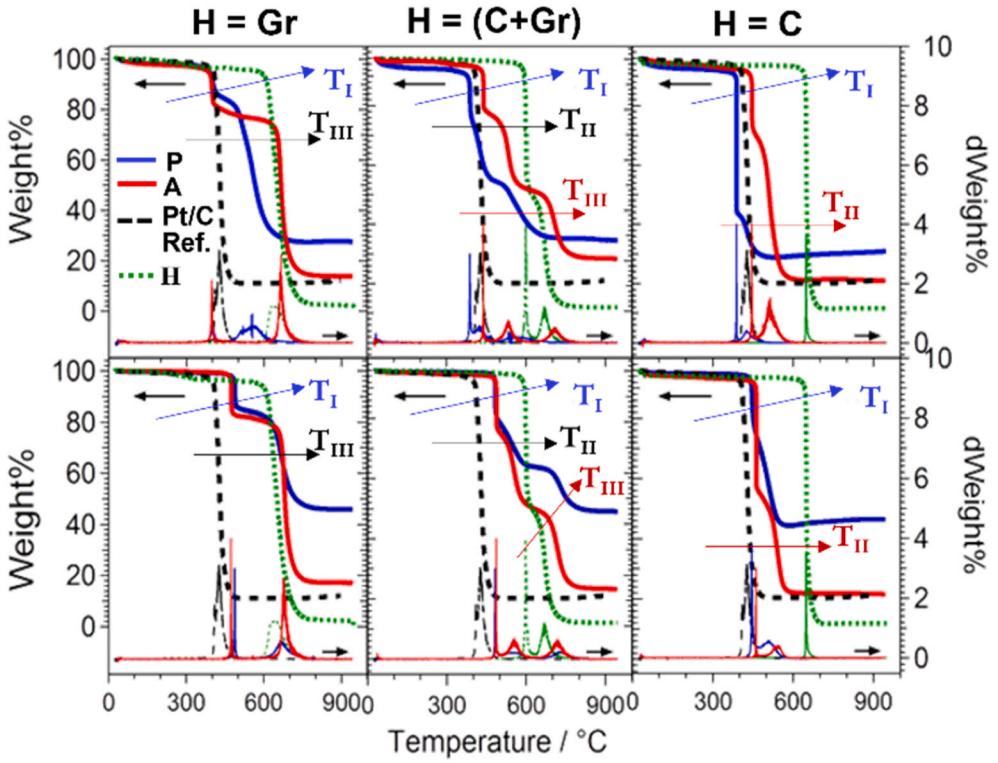

Fig. 4. HR-TGA in air of the pristine (blue lines) and activated (red lines) ECs, treated at $T_f = 600$ °C (top) and $T_f = 900$ °C (bottom). Comparison with HR-TGA of Pt/C ref. EC (black dashed lines) and of the supports **H** (green dotted lines). (For interpretation of the references to colour in this figure legend, the reader is referred to the Web version of this article.)

In activated ECs, lower residues at high temperature are measured than in pristine ECs, further demonstrating that the activation step removes the labile metal species included in the ECs.

3.3. Structure and morphology analysis

Confocal micro-Raman analysis shows that all ECs exhibit highly disordered CN *shells* (Figs. S10–S12). For **H = C** and **(C + Gr)**, the D band corresponding to the carbon in the *core* overlaps with the D band of carbon in the CN *shell*. On the other hand, Gr exhibits a very small D band due to a much lower degree of disorder in the graphene layers. Thus, as expected, the ratio between the intensities of the D and G bands (I_D/I_G) decreases upon increasing the fraction of Gr in **H**. In addition, I_D/I_G decreases upon activation for ECs containing Gr in the *core*, and it is lower in the ECs treated at higher T_f. This analysis confirms that the graphitization of the CN *shell* is improved at high T_f and by activating the ECs, in line with HR-TGA and composition studies.

Wide angle X-ray diffraction (WAXD) measures support that Ni-rich metal particles are etched during the electrochemical activation process (Figs. S13–S16). Rietveld analysis indicates that the amount of Ni-rich particles was 1.4–3 times higher in pristine ECs treated at higher T_f (Table S5). Nevertheless, the activation completely removes Ni-rich nanostructures and Ni NPs from $PtNi_{10}$-CN_l**900/H**(A), whereas traces of Ni NPs remain in $PtNi_{10}$-CN_l**600/H**(A). WAXD profiles of $PtNi_{10}$-CN_l**900/H**(A) reveal an fcc Pt_xNi phase ($3.5 < x < 5$) with a grain size on the order of 2–3 nm (see Figs. S13–S16 and Table S5), that was detected neither in the corresponding pristine samples nor in the $PtNi_{10}$-CN_l**600/H** and $PtNi_{10}$-CN_l**600/H**(A) ECs. It is expected that this Pt_xNi phase plays a crucial role to bestow the ECs with a high ORR performance [17,47].

High resolution scanning electron microscopy (HR-SEM) images elucidate the effect of the support nature, T_f and activation on the morphology of the ECs (Fig. 5A and Fig. S18). In the case of **H = C**, aggregates of C particles constituting the *core* are covered by a rough CN matrix (Fig. 5A), in agreement with previously reported *core-shell* CN-based ECs [32]. No substantial changes are observed upon activation, but micrometric Ni-based particles are removed (Fig. S18). For **H = Gr**, $PtNi_{10}$-CN_l**600/Gr** presents Gr flakes covered by a cratered CN *shell*. The craters, with a size of *ca*. 100 nm, likely originated from the removal of labile species during the synthesis (Fig. 5A). In $PtNi_{10}$-CN_l**900/Gr**, the CN *shell* uniformly covers the Gr flakes. Upon activation, the etching of labile species leaves some craters in the CN *shell*. In the case of **H = (C + Gr)**, C NPs decorate the Gr flakes and both are covered by a homogeneous *shell*, regardless of T_f. Gr flakes have a lateral dimension of over 500 nm, while C NPs show a diameter of ~50 nm (Fig. 5A). Upon activation, $PtNi_{10}$-CN_l**600/H**(A) ECs exhibit no significant change in morphology, however micrometric Ni-based particles are absent (Fig. S18). For all the ECs treated at $T_f = 900$ °C, the pristine materials present micrometric Pt_xNi grains that are effectively etched during the activation step, leaving heavily cratered CN *shells* (Fig. S18).

The morphology of the hierarchical $PtNi_{10}$-CN_l**900/(C + Gr)** is further analyzed by high-resolution transmission electron microscopy (HR-TEM), before and after activation (Fig. 5B and Figs. S19–S20). In the pristine EC, C and Gr are well-blended in the *core* (Fig. S19). The metal particles comprise: (i) micrometric Pt_xNi ($x \ll 1$) crystals; (ii) very rough Pt_xNi nanostructures (Fig. 5B–I); and (iii) Pt_xNi NPs (Fig. S19). Upon activation, C and Gr remain blended, while large Pt_xNi crystals are not present (Fig. S20). Metal active sites are present in small amount as Pt_xNi NPs (size d = 2, 5 nm, Fig. 5B–II), together with several Pt_xNi nanoclusters (Fig. 5B–III and Fig. S20) stabilized by the CN *shell*.

3.4. Performance analysis via the CV-TF-RRDE method

The electrochemical performance of the activated core-shell ECs is determined in both an acid and an alkaline environment (0.1 M $HClO_4$ and 0.1 M KOH, respectively). Cyclic voltammetry in inert N_2 atmosphere of $PtNi_{10}$-CN_l**600/H**(A) ECs shows no peaks associated to either H adsorption/desorption or PtO_x formation/reduction (Fig. S21), indicating the low incidence of Pt(0) on the ECs' surface, in agreement with

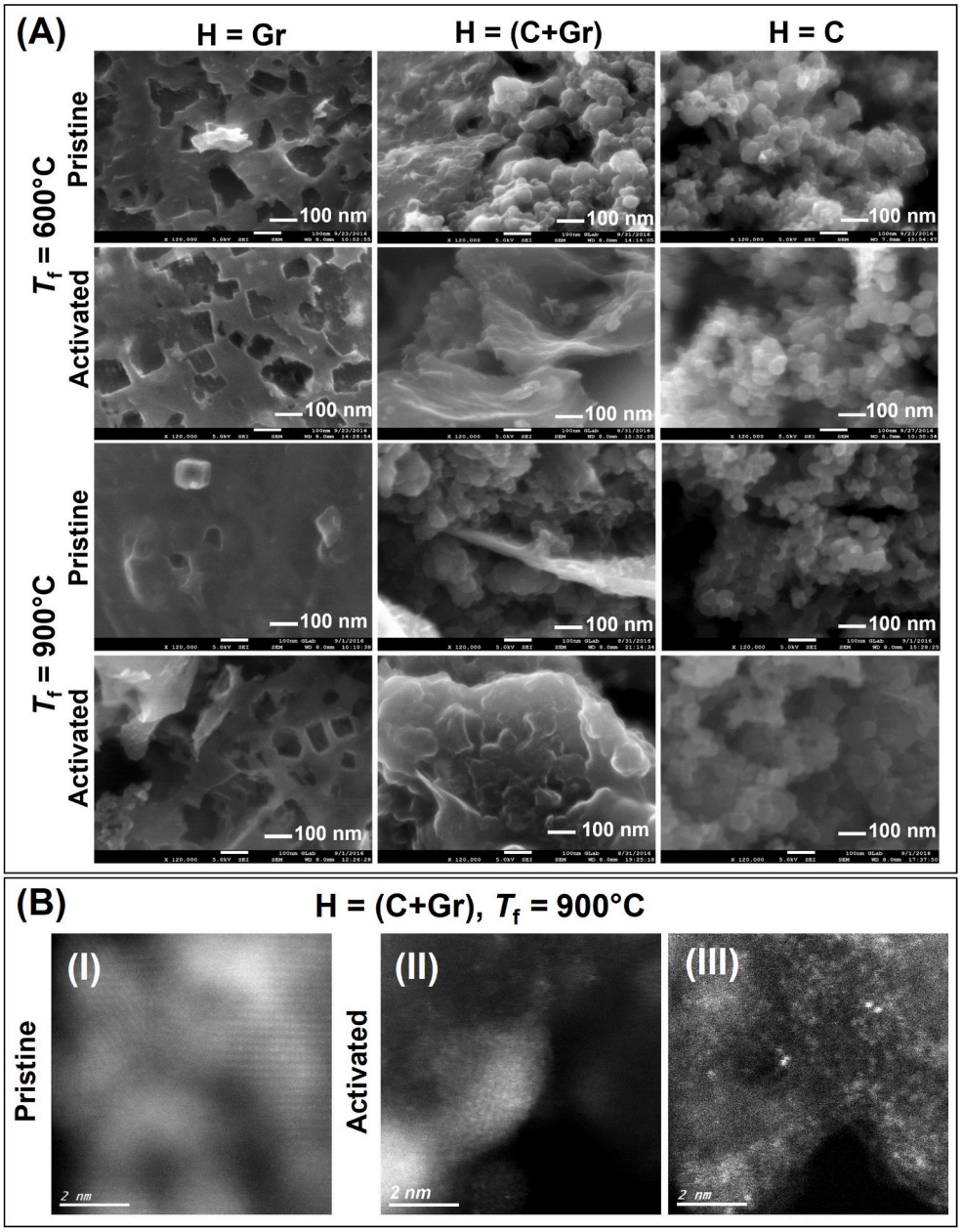

Fig. 5. (A) HR-SEM images of pristine and activated $PtNi_{10}$-CN_l**T_f/H** ECs; (B) HR-TEM images of pristine (I) and activated (II, III) $PtNi_{10}$-CN_l**900/(C + Gr)**.

HR-XPS measurements (see Fig. S3). In contrast, $PtNi_{10}$-CN_l**900/H**(A) ECs exhibit the typical peaks associated to Pt(0). Importantly, the signals ascribed to PtO_x formation/reduction are shifted to 20–40 mV higher potentials compared to the Pt/C ref. This evidence is ascribed to bifunctional/electronic effects triggered by the Ni "*co-catalyst*" and CN matrix, that inhibit the clogging of Pt surface species by oxygen adsorbates and are associated to the improved ORR kinetics in comparison with the Pt active sites of the Pt/C ref.

In CO stripping experiments (Fig. S22), no adsorption of CO is detected on $PtNi_{10}$-CN_l**600/H**(A) ECs, further demonstrating the low incidence of Pt(0) on the surface, as platinum is mostly coordinated by other ligands. On $PtNi_{10}$-CN_l**900/H**(A) ECs, multiple CO stripping peaks are revealed, shifted to lower potentials compared to the Pt/C ref. The stripping peaks are attributed to different active site chemistries on the surface of Pt_xNi NPs, as follows: (i) a small CO pre-oxidation peak is detected at 0.5 V *vs.* RHE in 0.1 M $HClO_4$ and 0.440 V *vs.* RHE in 0.1 M KOH, which is attributed to Pt_xNi particles with the lowest x value, embedded in *coordination nests* with a high density of N functionalities; (ii) a peak centered at 0.670 V and 0.580 V *vs.* RHE in acid and alkaline medium, respectively, is ascribed to Pt active sites on Pt_xNi NPs with an intermediate x value and lower density of N functionalities in the *coordination nests*; and (iii) a sharp peak at 0.715 V and 0.655 V *vs.* RHE in acid and alkaline medium, respectively, is assigned to active sites in Pt_xNi with the highest x and coordination of N atoms. It the alkaline medium, all peaks in the studied ECs and in the Pt/C ref. are shifted to lower potentials due to the easier displacement of adsorbed CO by abundant –OH groups, also originating from the environment. The observed potential shifts result from the combination of: (i) an electronic effect, obtained by alloying Pt with Ni and coordinating the metal sites by N ligands in *coordination nests* in the CN *shell*, thus decreasing the activation energy for the oxidation of CO_{ads} molecules; and (ii) a bifunctional effect, due to the presence of Ni atoms in Pt_xNi NPs that are easily covered by –OH functionalities, especially in alkaline conditions, which act to facilitate both the electrooxidation of CO_{ads} on neighboring

Pt sites, and the elimination of oxidation products [32]. $PtNi_{10}$-CN_l**900/H**(A) ECs exhibit ECSA values comparable to the Pt/C ref. (Fig. 6B), with the highest values measured for **H = (C + Gr)**, reaching 105 $m^2_{Pt}{\cdot}g^{-1}_{Pt}$ in 0.1 M $HClO_4$ and 69.3 $m^2_{Pt}{\cdot}g^{-1}_{Pt}$ in 0.1 M KOH. Lower ECSA values are consistently obtained in the alkaline medium due to the formation of oxides blocking the active sites.

The ORR profiles of $PtNi_{10}$-CN_l**600/H**(A) ECs show very poor performance in acid environment, which improves in alkaline medium, but remains inferior in comparison to the Pt/C ref. (Fig. 6A). This is consistent with the presence of active sites based on Pt(Ox) (Fig. 3), where O_2 species adsorb with difficulty. Conversely, $PtNi_{10}$-CN_l**900/H**(A) ECs show largely improved performance, particularly in the acid medium, with the ORR onset potential by 50–57 mV lower in comparison to the Pt/C ref. The ORR onset potential is determined as the $E(j_{Pt}(5\%))$, *i.e.* the potential at which the current density is equal to 5% of the diffusion-limited ORR current density of the Pt/C ref. EC [28]. In both environments, the ORR overpotential increases in the order $PtNi_{10}$-CN_l**900/H**(A) < Pt/C ref. ≪ $PtNi_{10}$-CN_l**600/H**(A). For the ECs treated at $T_f = 900$ °C, the ORR overpotential varies with **H** in the order **(C + Gr) < C < Gr**. Though the ORR diffusion-limited current is relatively low for **H = Gr**, possibly to an inhibited transport of O_2 from the bulk electrolyte to the active sites buried between Gr layers, such current is higher and comparable with the one of Pt/C ref. for **H = (C + Gr)** and **C**. In 0.1 M KOH, the performance of $PtNi_{10}$-CN_l**900/H**(A) ECs is slightly worse than in acid medium, but exhibited the same trends with the nature of **H**. An ORR event ascribed to Ni active sites was detected at ~0.7 V *vs.* RHE. The Tafel plots highlight the poor ORR kinetics of $PtNi_{10}$-CN_l**600/H**(A) ECs, which is somewhat improved in the alkaline environment (Fig. S23). $PtNi_{10}$-CN_l**900/H**(A) ECs show an ORR mechanism similar to that of the Pt/C ref., and only slightly affected by the pH of the medium. The selectivity for the $4e^-$ mechanism of ORR increases as T_f is raised (Fig. 6A and Fig. S24). For $PtNi_{10}$-CN_l**900/H**(A) ECs, the selectivity increases in the order **Gr < (C + Gr) < C** < Pt/C ref. (see Fig. S25). It is further noted that, in an alkaline environment, the selectivity of $PtNi_{10}$-CN_l***T*$_f$/H**(A) in the $4e^-$ ORR mechanism is much lower than that of the Pt/C ref. (see Fig. S25). This evidence is rationalized admitting that:

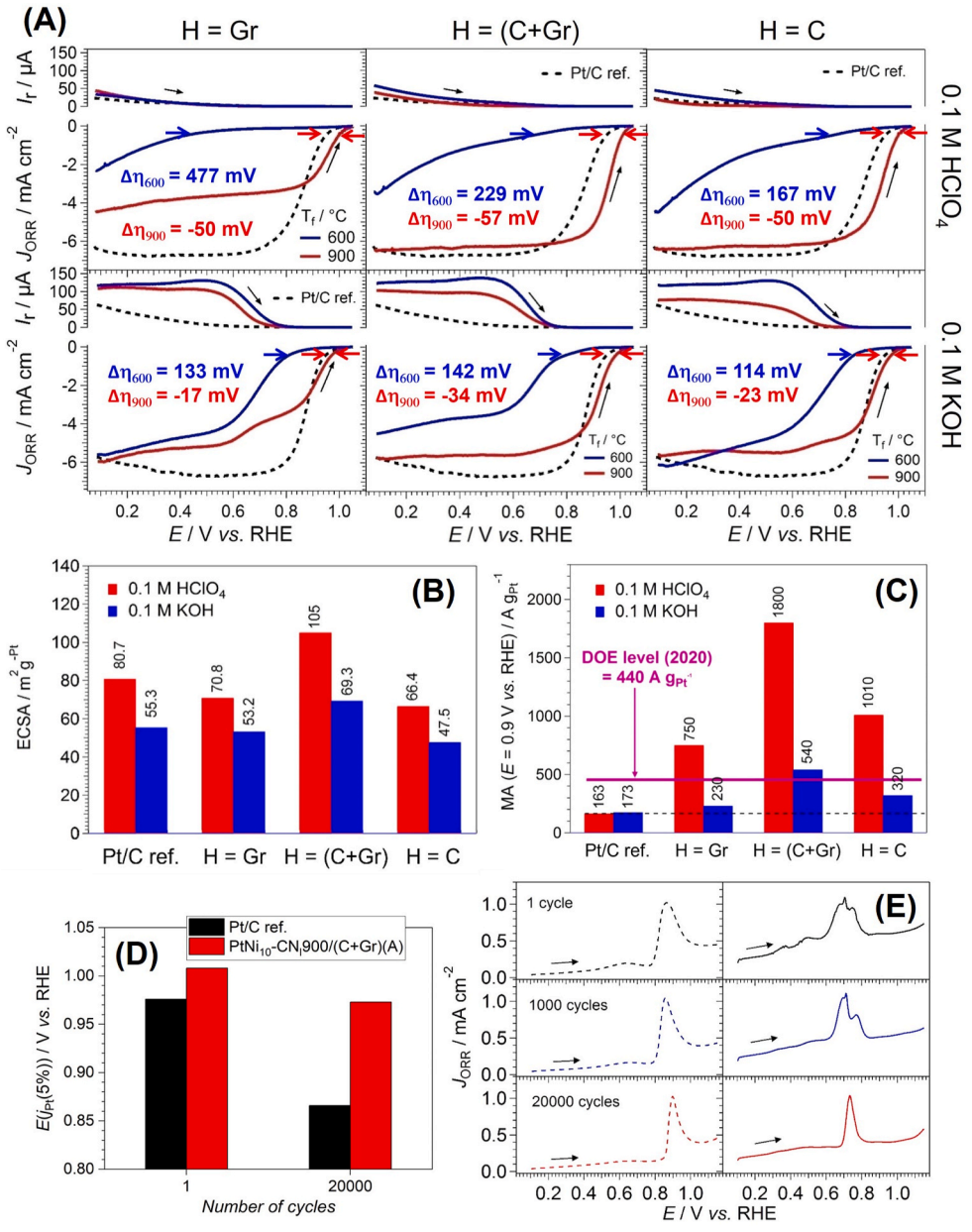

Fig. 6. (A) ORR profiles of activated ECs and comparison with Pt/C ref. in both acid (top) and alkaline (bottom) media, in an O_2 atmosphere. Voltammograms were recorded at a scan rate of 20 mV s^{-1}, a rotating speed of 1600 rpm and T = 25 °C. The loading of Pt on the disk electrode tip was 15 μg·cm^{-2}. The ring current is collected by polarizing the electrode at 1.2 V vs. RHE. (B) Comparison of ECSA values of $PtNi_{10}$-CN_l**900/H**(A) ECs and Pt/C ref. in acid and alkaline environments. (C) Mass activity comparison of $PtNi_{10}$-CN_l**900/H**(A) ECs and Pt/C ref. in acid and alkaline environments, measured at $E = 0.9$ V vs RHE. (D,E) Long-term performance of $PtNi_{10}$-CN_l**900/(C + Gr)**(A) and Pt/C ref. during the durability test conducted in 0.1 M $HClO_4$: (D) variation in $E(j_{Pt}(5\%))$ after 20000 cycles; (E) CO stripping profiles recorded after 1, 1000 and 20000 cycles.

(i) in $PtNi_{10}$-CN_l**600/H**(A) the ORR active sites mostly comprise Pt (Ox) and Ni(II) species, on which O_2 adsorbs with difficulty (especially in an acidic environment) thus yielding a high overpotential and a low selectivity in the 4e- ORR mechanism [17, 48];

(ii) in $PtNi_{10}$-CN_l**900/H**(A) a significant surface concentration of Ni and heteroatoms is still present in the active sites, possibly also due to stabilization by means of the *coordination nests*. Especially at alkaline pH, this would promote the adsorption of oxygenated species, reducing the number of couples of neighboring surface Pt (0) sites that are associated with a high selectivity in the 4e- ORR mechanism [38].

(iii) the presence of Gr in H actually promotes the stabilization of Ni and heteroatoms species in the active sites both in an acidic and in an alkaline environment, thus lowering the selectivity in the 4e- ORR mechanism.

In summary, a second pyrolysis temperature of 600 °C is insufficient to provide ECs with adequate ORR activity. Indeed, only little platinum is reduced to ORR active Pt(0) (see Fig. S3). Conversely, a higher pyrolysis temperature of 900 °C promotes the reduction of Pt(Ox) to Pt(0) and enables to obtain hierarchical *core-shell* CN-based ECs exhibiting superior performance with respect to the Pt/C ref. In acid medium, the mass activity @ 0.9 V (MA, Fig. 6C) of $PtNi_{10}$-CN_l**900/Gr**(A), $PtNi_{10}$-CN_l**900/C**(A), and $PtNi_{10}$-CN_l**900/(C + Gr)**(A) is respectively 1.7, 2.3 and 4.1 times higher than the U.S. DOE 2020 target (440 $A{\cdot}g_{Pt}^{-1}$ at 0.9 V). Though this latter benchmark actually refers to the performance of a single PEMFC and not to the outcome of CV-TF-RRDE measurements, it was deemed a useful figure to enable the general reader to understand the relevance of the results reported in this work in the framework of the state of the art. In both alkaline and acidic environment, the nature of the *core* affects the performance, which improves in the order **H = Gr < C < (C + Gr)**. In the **(C + Gr)** support, the different morphological features of Gr and C NPs synergistically act to improve the active sites dispersion, resulting in very large ECSA values (Fig. 6B) and high surface activity (Fig. S26). Moreover, $PtNi_{10}$-CN_l**900/(C + Gr)**(A) exhibits the lowest surface ratio of Pt and Ni atoms ($n_{Pt}/n_{Ni} = 0.29$, as measured by XPS, Fig. 3), thus maximizing the bifunctional effect and promoting the ORR kinetics.

The durability with respect to the Pt/C ref. of the best-performing EC, $PtNi_{10}$-CN_l**900/(C + Gr)**(A), was evaluated by accelerated durability tests [37]. In comparison with the Pt/C ref., the $E(j_{Pt}(5\%))$ of $PtNi_{10}$-CN_l**900/(C + Gr)**(A) is > 30 mV higher (Fig. 6D and Fig. S27). After 20000 cycles, the performance of the Pt/C ref. collapses with its $E(j_{Pt}(5\%))$ shifting to 110 mV lower value. In contrast, the $E(j_{Pt}(5\%))$ of $PtNi_{10}$-CN_l**900/(C + Gr)**(A) shifted to only 35 mV lower value, remaining considerably higher than the one of the Pt/C ref., and thus demonstrating a significantly enhanced durability. CO stripping experiments after 1000 and 20000 cycles (Fig. 6E) show the progressive disappearance of the peaks at lower potential values in $PtNi_{10}$-CN_l**900/(C + Gr)**(A). This phenomenon is attributed to the preferential dissolution of the non-noble metal [49], whereby Ni species are partially removed from the CN *shell* of the EC during cycling.

3.5. Performance in single PEMFC

The ECs treated at T_f = 900 °C and the Pt/C ref. are employed to fabricate *"proof of concept"* MEAs that are tested in a single PEMFC configuration, under operating conditions. The Pt loading in the electrocatalytic layer is 0.1 $mg_{Pt}{\cdot}cm^{-2}$ for the *core-shell* ECs and 0.5 $mg_{Pt}{\cdot}cm^{-2}$ for Pt/C ref. In the kinetic regime, the ECs exhibit significantly improved performance in comparison with the Pt/C ref. (Fig. S28), displaying 30–40 mV lower ORR overpotential values, in agreement with the CV-TF-RRDE results. The operating potentials at 50 $A{\cdot}g_{Pt}^{-1}$, that are adopted as a figure of merit for the ORR kinetics of the ECs in single PEMFC [20] are reported in Fig. 7A and Table S6. In single PEMFC, the ORR overpotential decreases in the order Pt/C ref. > **H = Gr > (C + Gr) > C**. By decreasing the back pressure from 4 to 1 bar, the ORR overpotentials of both the *core-shell* ECs and Pt/C ref. decreases by *ca.* 50 mV, while a 30 mV decrease is observed when switching from O_2 to air as the oxidant. The Tafel slopes evidence that the ORR mechanism for the *core-shell* ECs is similar to that of the Pt/C ref. (Fig. S29), in line with the CV-TF-RRDE analysis. Under O_2 flow, the Tafel slopes increase with decreasing the back pressure, due to a lower coverage of the Pt surface with O-based adsorbates. In air, the Tafel slopes of the $PtNi_{10}$ ECs are *ca.* 10 $mV{\cdot}decade^{-1}$ lower than the ones of the Pt/C ref., indicating that in the proposed ECs a higher fraction of active sites is covered by O-based adsorbates, likely due to a relatively high "oxophilicity" of Ni atoms in alloy NPs. These trends are interpreted considering that lower Tafel slopes are associated with a higher coverage of O-based adsorbates [41].

The polarization curves (Fig. S30) show that above the kinetic regime the slope increases in the order Pt/C ref. < **H = C < (C + Gr) < Gr**. The MEA performance of $PtNi_{10}$-CN_l**900/H**(A) is hindered by charge and mass transport phenomena, but improves with increasing the fraction of C in **H**. The introduction of C NPs in Gr supports acts to inhibit the close packing of graphene layers and the related ohmic drop in the electrocatalytic layers of MEAs [50]. Moreover, despite the low Pt loading at the cathode relatively high current densities are achieved for all *core-shell* $PtNi_{10}$ ECs, resulting in specific power values of 2.5–4 $kW{\cdot}g_{Pt}^{-1}$ at high back pressure of O_2 (Fig. 7B and Fig. S31). The transport ability toward active sites is also evaluated, by calculating the accessibility parameter Ψ (Table S7) [3]. The higher values of Ψ obtained for tested ECs relative to the Pt/C ref. suggest that the accessibility of

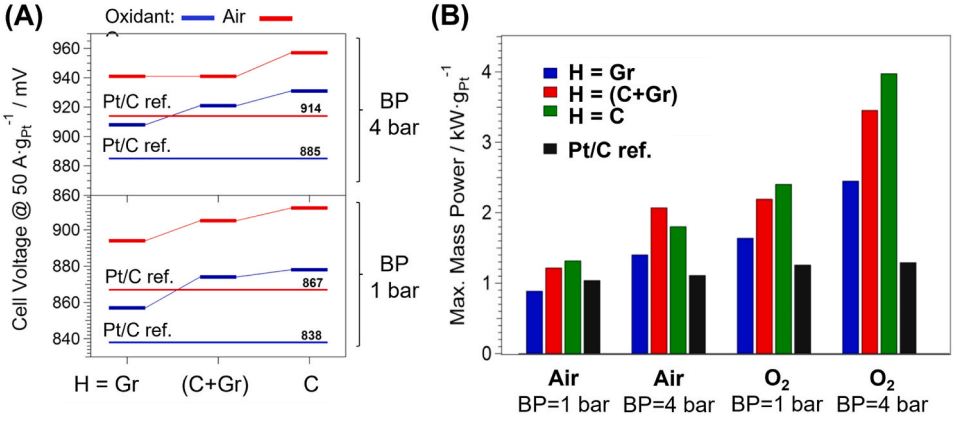

Fig. 7. Figures of merit for the performance of single PEMFCs mounting at the cathode either a $PtNi_{10}$-CN_l**900/H**(A) or Pt/C ref electrocatalysts: (A) cell voltage determined at 50 $A{\cdot}g_{Pt}^{-1}$; (B) maximum value of specific power of studied ECs.

reagents to the active sites is partially hindered by the morphology. In summary, single PEMFC tests indicate that hierarchical CN-based Pt–Ni ECs are promising, however additional efforts are needed to optimize the formulation of the cathodic electrocatalytic layer in order to address issues associated with mass transport phenomena, particularly under air flow and at low back pressures.

4. Conclusions

The main pyrolysis temperature, the activation step and the support *core* strongly affect the morphology and electrochemical performance of *core-shell* Pt–Ni carbon nitride ECs for the oxygen reduction reaction (ORR). The graphitization of CN shells is maximized at $T_f = 900$ °C. HR-XPS shows that $T_f = 600$ °C is too low to ensure a sufficient reduction of Pt(Ox) to ORR-active Pt(0), thus the resulting ECs demonstrated very poor ORR performance. $T_f = 900$ °C promotes the formation of Pt(0) and favors the segregation of the Pt on the CN *shells* surface, improving the exposure of active sites to O_2. The electrochemical dealloying-activation step removes labile Ni species and other impurities from the Pt_xNi active sites, as confirmed by WAXD, HR-SEM and HR-TGA analysis.

The $E(j_{Pt}(5\%))$ value determined by CV-TF-RRDE of $PtNi_{10}$-CN_l**900/H**(A) is 50–57 mV higher than that of a commercial Pt/C ref. in acid medium, with comparable selectivity in the $4e^-$ ORR mechanism. The mass activity of $PtNi_{10}$-CN_l**900/Gr**(A), $PtNi_{10}$-CN_l**900/C**(A), and $PtNi_{10}$-CN_l**900/(C + Gr)**(A) is respectively 1.7, 2.3 and 4.1 times higher than the U.S. DOE 2020 target (440 $A \cdot g_{Pt}^{-1}$ at 0.9 V). When both Gr and C are present in **H**, the active sites are better dispersed and enriched in Ni atoms, promoting the ORR kinetics through both electronic and bifunctional effects. HR-SEM analysis of $PtNi_{10}$-CN_l**900/(C + Gr)**(A) highlighted the hierarchical morphology with blended Gr and C NPs in the *core*. The latter was covered by the CN *shell* embedding Pt_xNi NPs and Pt_xNi nanoclusters (see HR-TEM images). The strong stabilization provided by the carbon nitride matrix in NPs *"coordination nests"* yields a high durability, with a loss of only *ca.* 35 mV in the $E(j_{Pt}(5\%))$ value upon 20000 cycles, while the Pt/C ref. shows a loss of over 100 mV.

In single *"proof of concept"* PEMFCs, $PtNi_{10}$-CN_l**900/H**(A) demonstrates a promising performance at low Pt loading (0.1 $mg_{Pt} \cdot cm^{-2}$ at the cathode). At 4 bar back pressure of O_2, specific power values up to 4 $kW \cdot g_{Pt}^{-1}$ are obtained. The performance under air flow and 1 bar back pressure is to be improved by optimizing MEA fabrication parameters. Nevertheless, the reported correlations among synthesis conditions, support composition, morphology and the electrochemical performance of hierarchical Pt–Ni ECs based on CN *shells* are crucial to guide the design of low-Pt ECs for PEMFCs that meet the targets of ORR activity and durability for practical applications.

CRediT authorship contribution statement

Francesca Lorandi: Writing – original draft, Formal analysis. **Keti Vezzù:** Investigation, Formal analysis. **Angeloclaudio Nale:** Investigation, Formal analysis. **Gioele Pagot:** Investigation, Formal analysis. **Yannick H. Bang:** Investigation. **Enrico Negro:** Methodology, Formal analysis, Writing – review & editing. **Vito Di Noto:** Conceptualization, Supervision, Funding acquisition, Formal analysis, We thank you very much for your consideration and look forward to hearing from you.

Declaration of competing interest

The authors declare that they have no known competing financial interests or personal relationships that could have appeared to influence the work reported in this paper.

Data availability

Data will be made available on request.

Acknowledgements

This work was supported by: (a) the European Union's Horizon 2020 research and innovation programme under grant agreement 881603 - Graphene Flagship Core Project 3; (b) the project *"Advanced Low-Platinum hierarchical Electrocatalysts for low-T fuel cells - ALPE"* funded by EIT Raw Materials; (c) "*Alkaline membranes and (platinum group metals)-free catalysts enabling innovative, open electrochemical devices for energy storage and conversion - AMPERE"*, FISR 2019 project funded by the Italian Ministry of University and Research.

Appendix A. Supplementary data

Supplementary data to this article can be found online at https://doi.org/10.1016/j.jpowsour.2022.232390.

References

[1] B.G. Pollet, S.S. Kocha, I. Staffell, Curr. Opinion. Electrochem. 16 (2019) 90–95.
[2] I. Staffell, D. Scamman, A.V. Abad, P. Balcombe, P.E. Dodds, P. Ekins, N. Shah, K. R. Ward, Energy Environ. Sci. 12 (2019) 463–491.
[3] V. Di Noto, E. Negro, K. Vezzù, F. Bertasi, G. Nawn, Electrochem. Soc. Interface 24 (2015) 59.
[4] D. Papageorgopoulos, U.S. Department of energy (DOE) hydrogen program 2021 annual merit review proceedings. https://www.hydrogen.energy.gov/pdfs/review21/plenary8_papageorgopoulos_2021_o.pdf last access: November 1st, 2022.
[5] U.S. DOE, Fuel cell technologies office multi-year research, development, and demonstration plan - section 3.4 fuel cells. https://www.energy.gov/sites/default/files/2017/05/f34/fcto_myrdd_fuel_cells.pdf last access: November 1st, 2022.
[6] S. Bobba, S. Carrara, J. Huisman, F. Mathieux, C. Pavel, European Commission, 2020. Brussels, Belgium.
[7] S. Sui, X. Wang, X. Zhou, Y. Su, S. Riffat, C.-j. Liu, J. Mater. Chem. 5 (2017) 1808–1825.
[8] J. Zhang, Y. Yuan, L. Gao, G. Zeng, M. Li, H. Huang, Adv. Mater. 33 (2021), 2006494.
[9] R.L. Borup, J.R. Davey, F.H. Garzon, D.L. Wood, M.A. Inbody, J. Power Sources 163 (2006) 76–81.
[10] J. Zhao, Z. Tu, S.H. Chan, J. Power Sources 488 (2021), 229434.
[11] J. Greeley, I. Stephens, A. Bondarenko, T.P. Johansson, H.A. Hansen, T. Jaramillo, J. Rossmeisl, I. Chorkendorff, J.K. Nørskov, Nat. Chem. 1 (2009) 552–556.
[12] I.E. Stephens, A.S. Bondarenko, U. Grønbjerg, J. Rossmeisl, I. Chorkendorff, Energy Environ. Sci. 5 (2012) 6744–6762.
[13] V. Di Noto, E. Negro, Electrochim. Acta 55 (2010) 7564–7574.
[14] K. Artyushkova, S. Pylypenko, M. Dowlapalli, P. Atanassov, J. Power Sources 214 (2012) 303–313.
[15] A. Ly, T. Asset, P. Atanassov, J. Power Sources 478 (2020), 228516.
[16] X. Ren, Q. Lv, L. Liu, B. Liu, Y. Wang, A. Liu, G. Wu, Sustain. Energy Fuels 4 (2020) 15–30.
[17] E. Negro, K. Vezzù, F. Bertasi, P. Schiavuta, L. Toniolo, S. Polizzi, V. Di Noto, Chemelectrochem 1 (2014) 1359–1369.
[18] M. Oezaslan, F. Hasché, P. Strasser, J. Phys. Chem. Lett. 4 (2013) 3273–3291.
[19] E. Negro, A. Bach Delpeuch, K. Vezzu, G. Nawn, F. Bertasi, A. Ansaldo, V. Pellegrini, B. Dembinska, S. Zoladek, K. Miecznikowski, Chem. Mater. 30 (2018) 2651–2659.
[20] V. Di Noto, E. Negro, A. Nale, P.J. Kulesza, I.A. Rutkowska, K. Vezzù, G. Pagot, Electrocatalysis 11 (2020) 143–159.
[21] V. Di Noto, E. Negro, B. Patil, F. Lorandi, S. Boudjelida, Y.H. Bang, K. Vezzù, G. Pagot, L. Crociani, A. Nale, ACS Catal. 12 (2022) 12291–12301.
[22] M. Pourbaix, Atlas of Electrochemical Equilibria in Aqueous Solutions, National Association of Corrosion Engineers, 1966.
[23] S. Komini Babu, T. O'Brien, M.J. Workman, M. Wilson, R. Mukundan, R. Borup, J. Electrochem. Soc. 168 (2021).
[24] F. Zhu, A. Wu, L. Luo, C. Wang, F. Yang, G. Wei, G. Xia, J. Yin, J. Zhang, Fuel Cell. 20 (2020) 196–202.
[25] P. Strasser, S. Kühl, Nano Energy 29 (2016) 166–177.
[26] B. Han, C.E. Carlton, A. Kongkanand, R.S. Kukreja, B.R. Theobald, L. Gan, R. O'Malley, P. Strasser, F.T. Wagner, Y. Shao-Horn, Energy Environ. Sci. 8 (2015) 258–266.
[27] V. Di Noto, E. Negro, A. Nale, G. Pagot, K. Vezzù, P. Atanassov, Curr. Opinion. Electrochem. 25 (2021), 100626.
[28] V. Di Noto, G. Pagot, E. Negro, K. Vezzù, P.J. Kulesza, I.A. Rutkowska, G. Pace, Curr. Opinion. Electrochem. 31 (2022), 100839.
[29] V. Di Noto, E. Negro, K. Vezzu, F. Bertasi, G. Nawn, L. Toncelli, S. Zeggio, F. Bassetto, Electrocatalysts on Carbonitride Matrices, Patent US10811691B2, 2020.
[30] V. Di Noto, E. Negro, A.B. Delpeuch, F. Bertasi, G. Pagot, Graphene and Other 2d Materials as Layered" Shells" Supported on" Core" Nanoparticle Carriers, patent US20190334179A1, 2019.
[31] V. Di Noto, E. Negro, R. Gliubizzi, S. Lavina, G. Pace, S. Gross, C. Maccato, Adv. Funct. Mater. 17 (2007) 3626–3638.
[32] V. Di Noto, E. Negro, Fuel Cell. 10 (2010) 234–244.

[33] Y. Garsany, O.A. Baturina, K.E. Swider-Lyons, S.S. Kocha, Anal. Chem. 82 (2010) 6321–6328.
[34] T. Schmidt, U. Paulus, H.A. Gasteiger, R. Behm, J. Electroanal. Chem. 508 (2001) 41–47.
[35] D. van der Vliet, D.S. Strmcnik, C. Wang, V.R. Stamenkovic, N.M. Markovic, M.T. M. Koper, J. Electroanal. Chem. 647 (2010) 29–34.
[36] H.A. Gasteiger, S.S. Kocha, B. Sompalli, F.T. Wagner, Appl. Catal. B Environ. 56 (2005) 9–35.
[37] A.N.L. National, Renewable energy laboratory (NREL), naval research laboratory, testing oxygen reduction reaction activity with the rotating disc electrode technique. https://www.energy.gov/sites/prod/files/2014/03/f12/webinarslides_rde_technique_031213.pdf. February 2022.
[38] V. Di Noto, E. Negro, S. Polizzi, F. Agresti, G.A. Giffin, ChemSusChem 5 (2012) 2451–2459.
[39] F. Bonaccorso, L. Colombo, G. Yu, M. Stoller, V. Tozzini, A.C. Ferrari, R.S. Ruoff, V. Pellegrini, Science 347 (2015), 1246501.
[40] B. Seger, P.V. Kamat, J. Phys. Chem. C 113 (2009) 7990–7995.
[41] S. Kabir, A. Serov, K. Artyushkova, P. Atanassov, ACS Catal. 7 (2017) 6609–6618.
[42] M.Z. Iqbal, S. Siddique, A. Khan, S.S. Haider, M. Khalid, Mater. Res. Bull. 122 (2020), 110674.
[43] E. Negro, A. Nale, K. Vezzù, G. Pagot, S. Polizzi, R. Bertoncello, A. Ansaldo, M. Prato, F. Bonaccorso, I.A. Rutkowska, Electrochim. Acta 280 (2018) 149–162.
[44] Y. Huang, Y. Chen, M. Xu, T. Asset, P. Tieu, A. Gili, D. Kulkarni, V. De Andrade, F. De Carlo, H.S. Barnard, A. Doran, D.Y. Parkinson, X. Pan, P. Atanassov, I. V. Zenyuk, Mater. Today 47 (2021) 53–68.
[45] H.W. Nesbitt, D. Legrand, G.M. Bancroft, Phys. Chem. Miner. 27 (2000) 357–366.
[46] J.F. Moulder, W.F. Stickle, P.E. Sobol, K.D. Bomben, Handbook of X-Ray Photoelectron Spectroscopy - A Reference Book of Standard Spectra for Identification and Interpretation of XPS Data, Perkin-Elmer Corporation, Physical Electronics Division, Eden Praire, Minnesota, USA, 1992.
[47] I. Matanovic, F.H. Garzon, N.J. Henson, J. Phys. Chem. C 115 (2011) 10640–10650.
[48] H.A. Hansen, J. Rossmeisl, J.K. Nørskov, Phys. Chem. Chem. Phys. 10 (2008) 3722–3730.
[49] V. Beermann, M.E. Holtz, E. Padgett, J.F. de Araujo, D.A. Muller, P. Strasser, Energy Environ. Sci. 12 (2019) 2476–2485.
[50] L. Işıkel Şanlı, V. Bayram, S. Ghobadi, N. Düzen, S. Alkan Gürsel, Int. J. Hydrogen Energy 42 (2017) 1085–1092.